



A comparative study of Pt and Pt–Pd core–shell nanocatalysts

Nguyen Viet Long^{a,b,c,d,*}, Michitaka Ohtaki^d, Tong Duy Hien^c, Jalem Randy^a, Masayuki Nogami^{a,**}

^a Department of Materials Science and Engineering, Nagoya Institute of Technology, Gokiso-cho, Showa-ku, Nagoya 466-8555, Japan

^b Posts and Telecommunications Institute of Technology, km 10 Nguyen Trai, Thanh Xuan, Ha Dong, Hanoi, Vietnam

^c Laboratory for Nanotechnology, Vietnam National University, Ho Chi Minh, Linh Trung, Thu Duc, Ho Chi Minh, Vietnam

^d Department of Molecular and Material Sciences, Interdisciplinary Graduate School of Engineering Sciences, Kyushu University, 6-1 Kasugakouen, Kasuga, Fukuoka 816-8580, Japan

ARTICLE INFO

Article history:

Received 29 April 2011

Received in revised form 15 July 2011

Accepted 20 July 2011

Available online 10 August 2011

Keywords:

Nanocatalysts

Core–shell bimetallic nanoparticles

Pt nanoparticles

Pt–Pd core–shell nanoparticles

Fast hydrogen adsorption, Direct methanol fuel cells (DMFCs)

ABSTRACT

This comparative study characterizes two types of metallic and core–shell bimetallic nanoparticles prepared with our modified polyol method. These nanoparticles consist of Pt and Pt–Pd core–shell nanocatalysts exhibiting polyhedral morphologies. The controlled syntheses of Pt metallic nanoparticles in the 10-nm regime (4–8 nm) and Pt–Pd bimetallic core–shell nanoparticles in the 30-nm regime (15–25 nm) are presented. To realize our ultimate research goals for proton exchange membrane fuel cells (PEMFCs) and direct methanol fuel cells (DMFCs), we thoroughly investigate the dependence of the electrocatalytic properties of the nanoparticles on the structure, size and morphology. Significant differences in the electrocatalysis are also explained in experimental evidences of both Pt and Pt–Pd nanocatalysts. We suggested that the core–shell controlled morphologies and nanostructures of the Pd nanoshell as the Pd atomic monolayers will not only play an important role in producing inexpensive, novel Pt- and Pd-based nanocatalysts but also in designing more efficient Pt- and Pd-based nanocatalysts for practical use in DMFC technology. Our comparative results show that Pt–Pd nanocatalysts with Pd nanoshells exhibited much better electrocatalytic activity and stabilization compared to Pt nanocatalysts. Interestingly, we found that the size effect is not as strong as the nanostructuring effect on the catalytic properties of the researched nanoparticles. A nanostructure effect of the core–shell bimetallic nanoparticles was identified.

© 2011 Elsevier Ltd. All rights reserved.

1. Introduction

Traditionally, Pt- or Pd-based nanocatalysts are developed with fuel cell (FC) technologies because they are highly active electrocatalysts for oxygen reduction reactions (ORR), methanol oxidation reactions (MOR) and ethanol oxidation reactions (EOR) [1–3]. These nanocatalysts are adopted in the cathodes and anodes of fuel cell systems [1–6]. Their electrocatalysis was derived from the surface-to-volume ratio and quantum-size effect. Additionally, a synergistic effect was discovered to be the cause of the enhanced catalytic activity [7]. At present, FC technologies cover a remarkably wide variety of practical applications. Typically, they include proton exchange membrane fuel cells (PEMFCs) and direct methanol fuel cells (DMFCs) [3–8]. In addition, alcohol fuels are utilized for

FCs. Unfortunately, the cost of Pt is still high, which has hindered the large-scale production and commercialization of these technologies. At present, Pt- or Pd-based nanocatalysts, combined with various types of carbon supports and polymer membranes, are employed in low and high temperature FC technologies, enabling promising FC technologies to be competitive [8–10]. Among them, DMFC technology has potential applications in portable devices, including cell phones and portable computers, and automobiles. For DMFC, methanol is one of the most widely used fuels because of its low toxicity and large abundance. The technology for methanol production has been well developed [1–3]. Today, Pt–Ru nanocatalysts that show good catalytic activity are successfully tested in DMFCs; however, the high cost of their commercialization remains a significant challenge [11,12,78]. Recently, an attractive method of using ultrasound for the fabrication of nanocatalysts has been tested in various FCs, showing the advantages of Pt–Ru nanocatalysts [13,78]. To achieve practical, cost-effective design, various types of new Pt-based catalysts have been developed as bimetallic alloys [11–13]. However, the successful synthesis of core–shell morphologies in the sub-30-nm regime is relatively rare. In addition, one of the great challenges for researchers in the field is the difficulty in fabricating the thin Pt shell as atomic monolayers on the definite core [14,15]. The common strategies of controlling the Pd–Pt bimetallic nanoparticles of the core–shell structure focus on

* Corresponding author at: Department of Materials Science and Engineering, Nagoya Institute of Technology, Gokiso-cho, Showa-ku, Nagoya 466-8555, Japan; Department of Molecular and Material Sciences, Interdisciplinary Graduate School of Engineering Sciences, Kyushu University, 6-1 Kasugakouen, Kasuga, Fukuoka 816-8580, Japan. Tel.: +81 090 9930 9504/81-(0)92 583 8835; fax: +81 092 583 8835/81 (0)92 583 8835.

** Corresponding author.

E-mail addresses: nguyenviet.long@yahoo.com, nguyenvietlong01@gmail.com (N.V. Long), nogami@nitech.ac.jp, mnogami@mtj.biglobe.ne.jp (M. Nogami).

studying the nature of the nanoparticles. Therefore, the techniques can be extended to cheap nanocores such as oxides, glasses, alloys, and ceramics to design new functional materials, which are potentially used for various FC systems [16–18]. In this paper, we report a simple and effective method of preparing precious metallic and bimetallic nanoparticles. Pt and Pt–Pd core–shell nanoparticles were synthesized with controlled structure, size and morphology by the reduction of H_2PtCl_6 and Na_2PdCl_4 in ethylene glycol (EG) using AgNO_3 as a structure-controlling agent. The methods of transmission electron microscopy (TEM) and high resolution (HR) TEM were adopted to characterize their morphology and size. The results showed that the size and morphology of Pt nanoparticles can be controlled with a small amount of AgNO_3 . The prepared Pt nanoparticles of 4–8 nm exhibited a polyhedral morphology. The Pt–Pd core–shell nanoparticles of 15–25 nm were controllably synthesized and exhibited polyhedral morphology. A comparison of their electrocatalysis was conducted to confirm the advantages of the polyhedral morphology and core–shell configuration. The significant catalytic enhancement and stabilization originating from the nanoshell layer were identified. Our results thereby revealed that a new strategy for creating nanostructured catalysts with high hydrogen solubility and reactivity as well as fast, sensitive, and stable hydrogen adsorption could be crucial for FCs.

2. Experimental

2.1. Synthesis of metallic and bimetallic nanoparticles

2.1.1. Chemicals for synthesis

In our synthesis, chemicals from Aldrich (or Sigma–Aldrich) were used in the experimental processes. These include polyvinylpyrrolidone (PVP, a protective reagent) (FW: 55,000), sodium tetrachloropalladate (II) hydrate (Na_2PdCl_4) (ACS reagent), and chloroplatinic acid hexahydrate (H_2PtCl_6) (ACS reagent), which are the precursors for producing Pt nanoparticles and Pt–Pd core–shell nanoparticles. Ethylene glycol (EG) was used as both the solvent and the reducing agent. Silver nitrate (metal basis) was used as a modifying agent. Solvents, including ethanol, acetone, and hexane, were used for washing and cleaning. A Narnstead H_2O purification system provided ionized, distilled, and milli-Q water. All chemicals were of analytical grade and were used without any further purification.

2.1.2. Synthesis of Pt metallic nanoparticles

To synthesize Pt nanoparticles (4–8 nm), 3 mL of EG, 1.5 mL of 0.0625 M H_2PtCl_6 , 3 mL of 0.375 M PVP, and 0.5 mL of 0.04 M AgNO_3 were used. The volumes of 4 mL of EG and 0.5 mL of 0.04 M AgNO_3 were mixed in a flask and heated to 160 °C. After the solution was mixed for 15 min, argon (Ar) gas was bubbled into the flask for 20 min prior to synthesis. The solution was refluxed for 2 h in an Ar gas atmosphere. Next, 20 μL of 0.0625 M H_2PtCl_6 was added to the flask at 160 °C, sequentially followed by the injection of 40 μL of 0.375 M PVP into the flask until 1.5 mL of 0.0625 M H_2PtCl_6 and 3 mL of 0.375 M PVP were added to the flask and reacted for 15 min under stirring. The ratio of the solution volumes of PVP and H_2PtCl_6 was 2:1 (40 μL /20 μL). The reduction of H_2PtCl_6 by EG occurred. The dark-brown mixture was stirred in the flask at 160 °C for 15 min. As a result, a dark-brown product of Pt nanoparticles was obtained.

2.1.3. Synthesis of Pt–Pd core–shell bimetallic nanoparticles

To synthesize Pt–Pd core–shell nanoparticles, Pt nanoparticles were made as the initial cores. In the synthesis of the Pt cores, 3 mL of EG, 1.5 mL of 0.0625 M H_2PtCl_6 , 3 mL of 0.375 M PVP, and 0.5 mL of 0.04 M AgNO_3 were used. The volumes of 3 mL of EG and 0.5 mL of 0.04 M AgNO_3 were mixed in a flask and heated to 160 °C. The solution was mixed for 15 min. Then, Ar gas was bubbled for

20 min prior to synthesis. The solution was refluxed for 2 h in an Ar gas atmosphere and sealed to prevent air from entering the flask. Next, 30 μL of 0.0625 M H_2PtCl_6 was added to the flask at 160 °C followed by 60 μL of 0.375 M PVP so that their total volumes, including 1.5 mL of H_2PtCl_6 and 3 mL of PVP, were reacted under stirring for 15 min. The volume ratio of PVP and H_2PtCl_6 was 2:1 (60 μL /30 μL), and it was observed that the fast reduction of H_2PtCl_6 by EG occurred. The resultant mixture was stirred in the flask at 160 °C for 15 min. As a result, a dark brown product containing Pt nanoparticles was obtained. In Section 2, Pt nanoparticles synthesized by the above reliable procedure were subsequently used as the prepared cores for producing Pt–Pd core–shell nanoparticles (15–25 nm). Here, 30 μL of 0.0625 M Na_2PdCl_4 was added to the flask at 160 °C, followed by 60 μL of 0.375 M PVP, so that their total volumes, including 1.5 mL of Na_2PdCl_4 and 3 mL of PVP, were reacted under stirring. The volume ratio of PVP and Na_2PdCl_4 was 2:1 (60 μL /30 μL). It was observed that the successive reduction of Na_2PdCl_4 by EG occurred under continuous stirring for 15 min. Subsequently, the resultant mixture was kept in the flask under stirring for some time ($t \sim 2$ –5 min) [19]. Then, the flask containing the product solution was moved out of the boiling-oil bath. Through this process, the only formation of Pt–Pd core–shell nanoparticles was obtained in our final product.

2.2. Electrocatalyst preparation

To obtain pure nanoparticles, the product containing the prepared Pt and Pt–Pd nanoparticles were washed with a triple volume of acetone, followed by centrifugation at 5000 rpm. Then, solid products were obtained and re-dispersed in ethanol/hexane (volume ratio $\sim 1:3$), and the mixtures were centrifuged at 3000 rpm. The PVP-encapsulated Pt and Pt–Pd nanoparticles were washed in ethanol/hexane several times. After washing, the nanoparticles were dispersed in milli-Q water to achieve a density of $\sim 1 \text{ mg mL}^{-1}$ with the aid of an ICPS analyzer. For electrochemical measurements, the working electrode was a glassy carbon rod (RA5, Tokai Carbon Co., Ltd., diameter: 5.2 mm). First, the electrode surface was cleaned and activated by using a polishing cloth (Buehler Textmet) and an Al slurry (Aldrich, particle size $\sim 50 \text{ nm}$), followed by copious washing with milli-Q water. This procedure was repeated until the surface looked like a mirror. Then, a fixed weight of the prepared catalyst loading was set onto the polished electrodes. The loaded electrodes were dried for 3 h at 25 °C and heated up to 450 °C in air to remove the organic species (heating rate $\sim 1 \text{ }^\circ\text{C min}^{-1}$, keeping time $\sim 2 \text{ h}$). The slow heating rate was used to avoid the sintering of the nanoparticles. After the electrode sintering heat treatment, the electrodes were slowly cooled and subsequently exposed to a H_2/N_2 (20%, 80%) flow at 100 °C for 3 h to reduce the existence of Pt–O and ensure a pristine catalyst surface. To improve mechanical stability and durability, 10 μL of 5 wt% Nafion solution was added onto the electrodes, and they were then dried overnight before electrochemical measurements.

2.3. Characterization

2.3.1. Transmission electron microscopy

To characterize the Pt nanoparticles of 4–8 nm and Pt–Pd core–shell nanoparticles of 15–25 nm, copper grids containing the Pt and Pt–Pd core–shell nanoparticles were maintained under vacuum by using a vacuum cabinet (JEOL–JEM–DSC10E Film Vacuum Desiccator Cabinet) prior to TEM and HRTEM measurements. The copper grids were treated again at a drying station (JEOL JDS-230F Drying Station) using an ion cleaner that employed glow discharge in vacuum to remove any contamination (Ion Cleaner JIC-410 JEOL). The copper grids were maintained overnight under high vacuum conditions in the transmission electron microscope

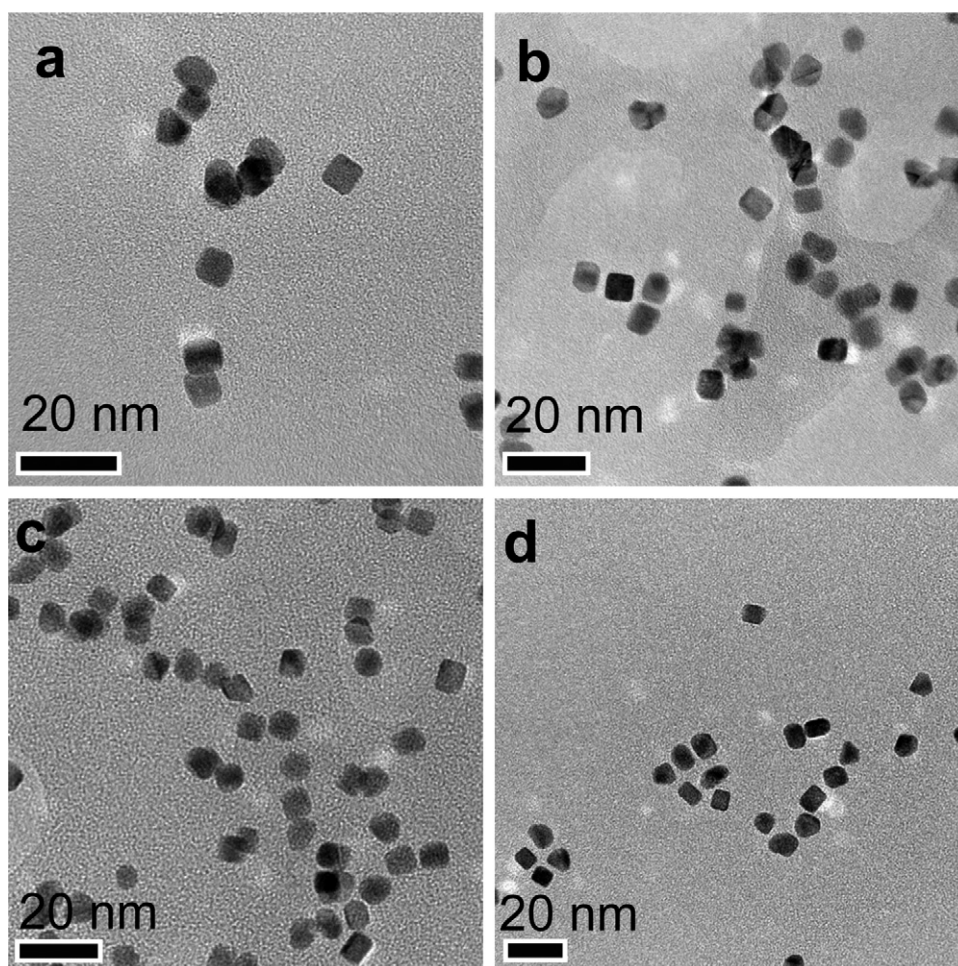


Fig. 1. TEM images of polyhedral Pt nanoparticles. Scale bars: (a)–(d) 20 nm.

(JEOL JEM-2100F or JEM-2010) prior to the TEM and HRTEM measurements. The TEM images were obtained using a transmission electron microscope (JEOL JEM-2100F and JEM-2010) operated at 200 kV. Finally, DigitalMicrograph software (Gatan, Inc.) was used in the TEM and HRTEM studies to acquire, visualize, analyze, and process the digital image data of the Pt and Pt–Pd nanoparticles.

2.3.2. Electrochemical measurements

A typical setup of a three-electrode electrochemical system was used in our cyclic voltammetry experiments at ambient room temperature. The electrodes were connected to a potentiostat (SI 1287 Electrochemical Interface, Solartron). The cell was a 50 mL glass vial, which was treated with a mixture of H_2SO_4 – HNO_3 solution and washed with milli-Q water. A leak-free $\text{AgCl}/\text{Ag}/\text{NaCl}$ electrode (RE-1B, ALS) served as the reference, and the counter electrode was a Pt coil (002234, ALS). All potentials were reported E vs. $(\text{Ag}/\text{AgCl})/\text{V}$. The electrolyte solution was bubbled with N_2 gas for 30 min before each measurement. The N_2 blanket was maintained throughout the course of potential sweeping. For the base voltammetry, the electrolyte was a solution of 0.5 M H_2SO_4 (or 0.5 M H_2SO_4 and 1 M CH_3OH). The potential window between $E = -0.2\text{ V}$ and $E = 1.0\text{ V}$ with a sweep rate of 50 mV s^{-1} was used. For the oxidation of methanol, 1.0 M methanol in milli-Q water was added to the electrolyte. The measurements were cycled until stable voltammograms were achieved. The electrochemical surface areas (ECSA) were estimated by considering the area under the curve in the hydrogen desorption region of the forward scan with respect to

the monolayer of hydrogen adsorbed onto the Pt–Pd nanocatalyst surfaces.

2.3.3. X-ray diffraction method

Starting from the products of the prepared Pt and Pt–Pd core-shell nanoparticles, 3 mL of an ethanolic solution of the prepared Pt nanoparticles or Pt–Pd core-shell nanoparticles was set onto the slides of special glass with a small area of approximately 1 cm^2 for the XRD method. The drops of the ethanolic solution of the prepared Pt and Pt–Pd core-shell nanoparticles were poured onto the glass substrate and dried at $80\text{ }^\circ\text{C}$ and $100\text{ }^\circ\text{C}$ for 6 h prior to use. These slides were treated with ethanol to remove any impurities. X-ray diffraction patterns were recorded by a diffractometer (X'Pert-Phillips) operating at 45 kV/45 mA and using $\text{Cu K}\alpha$ radiation (0.54056 nm). The specific crystal nanostructures of the prepared Pt and Pt–Pd core-shell nanoparticles were compared in detail.

3. Results and discussion

3.1. Structure, size and morphology of metallic and bimetallic nanoparticles

Fig. 1 shows the TEM images of the polyhedral Pt nanoparticles with particle sizes of 5–8 nm that were produced by the modified polyol method at $160\text{ }^\circ\text{C}$ for 15 min in the presence of PVP, with the assistance of AgNO_3 as the structure-controlling agent.

These Pt nanoparticles exhibited truncated polyhedral morphologies at the corners. Most of the Pt nanoparticles exhibit the main forms of cubic, octahedral, and tetrahedral morphologies. In addition, the truncated cubic, octahedral, and tetrahedral morphologies were also observed. It is certain that the addition of AgNO_3 influenced the shaping of the specific morphology of Pt nanoparticles associated with their short synthetic time. We estimate that this occurred at approximately 10–15 min. The polyhedral morphologies also show very sharp corners, edges, and facets. In all cases, the sharp and polyhedral Pt nanoparticles of the characteristic low and high-index planes were considered for their practical applications in catalysis [19–21]. They exhibited their various morphologies of $\{111\}$, $\{100\}$, and $\{110\}$ facets or other facets of various Pt $\{hkl\}$ planes. Therefore, a modified polyol with the assistance of AgNO_3 potentially offers viable ways to synthesize precious metal nanoparticles under size and morphology control [20]. The characterization of shape-dependent electrocatalytic activities of Pt nanostructures has been investigated [21–23]. The polyhedral morphology of low and high-index planes or various Pt $\{hkl\}$ planes exhibited a high electrocatalytic activity that offers an enhancement in ORR. The highest stability of methanol electro-oxidation by hydrogen adsorption and desorption was verified in the Pt nanoparticles with polyhedral shapes [24]. The polyhedral Pt nanoparticles exhibited good single-crystal structures that were controlled in both size and morphology. In addition, the twinned structures of the Pt nanoparticles were also observed. The results confirmed the polyhedral Pt nanoparticles in the homogenous single-crystal growth.

Fig. 2 shows the typical TEM and HRTEM images of the Pt–Pd core–shell nanoparticles that were 10–25 nm in size, synthesized by a polyol method in the presence of a trace amount of silver nitrate (0.5 mL of 0.04 M AgNO_3). The HRTEM images showed the segregation of the Pt core and Pd shell without their alloying. The Pd atomic monolayers in homogeneous nucleation and growth were observed in the layer-by-layer mechanism. These monolayers protect the polyhedral morphology of the initial Pt cores. This provides further evidence for the epitaxial shell growth mode. Fig. 2 also shows the HRTEM images of the Pt–Pd core–shell nanoparticles, and the vertically oriented overgrowth of Pd atomic monolayers on the Pt core is examined. The thickness of the Pd atomic monolayers was estimated to be less than 4 nm, and the overgrowth of these monolayers on the surface of the Pt core was due to the layer-by-layer gradual growth mechanism [4,19].

The oriented overgrowth of Pd atomic monolayers on the surface of the Pt nanocore showed a good lattice match. However, we suggest that the re-crystallization of metallic and bimetallic nanoparticles need to be studied at this stage. It is clear that Pt–Pd core–shell nanoparticles typically exhibit cubic, octahedral, and tetrahedral main core–shell morphologies. In this study, we successfully produced Pt–Pd core–shell nanoparticles (15–25 nm). In addition, we also observed that the Pd coatings (or the sharp and polyhedral Pd shells) of the Pt–Pd core–shell nanoparticles not only exhibit tetrahedral, cubic, and octahedral morphologies but also possess highly symmetric crystal structures. The polyhedral Pt cores were synthesized, which shaped the homogeneous nucleation and growth of the final morphology of the polyhedral Pd shells. In this mode, it can be suggested that the initial Pt nanocores shaped the overgrowth of the nanoshells of the Pd atomic monolayers. Here, the core–shell formation demonstrated the segregation of the Pt cores and Pd shells without any alloying phenomenon. The homogeneous and inhomogeneous nucleation and growth of the shell at the core and shell interface of two different metals is due to the epitaxial and/or non-epitaxial growth modes [4,19,25,26]. The two Pt and Pd metals have the same crystal structure (fcc). Therefore, the Pd shell could grow epitaxially on the Pt core because of their similar crystal structures [4,19]. In comparison with the

Pt core, the thickness of the Pd shell can be precisely manipulated by the quantity of the Na_2PdCl_4 precursor added. A classical theory was used to explain the nucleation and growth of metallic nanoparticles and was extended to study the nucleation and growth of alloy and core–shell bimetallic nanoparticles. Gibbs free energy and overall excess free energy were applied to understand issues of the sizes and morphologies of the nanoparticles, and synthesize uniform formations of the core and/or the shell. The nucleation and growth modes used include Frank–van der Merwe (FM), Volmer–Weber (VW), and Stranski–Krastanov (SK) modes. These enable us to explain the formations of various nanostructures of Pt, Pt–based alloys and Pt–based core–shell nanoparticles [4,19,27,28]. Thus, we need to control the various FM, VW, and SK growth modes experimentally during the reductions of two metallic salts. This strategy can lead to produce a homogeneous system of core–shell bimetallic nanoparticles, which strongly depends on controlling the dominant FM growth mode under certain experimental conditions. Therefore, homogeneous and inhomogeneous nucleation and growth was possibly achieved in the formation of the nanoshells. The case of homogeneous nucleation and growth of the shell by a layer-by-layer mechanism is a desired mode for a controlled synthesis. The important features of Pt–Pd core–shell nanoparticles consist of islands, terraces, and steps around the edges and monatomic steps [4,19]. Here, we have observed the uniformity of the directions of overgrowth of the Pd monolayer on the Pt core via a layer-by-layer mechanism and the lattice fringe for the Pd shell was estimated to be 0.246 nm. As shown in Fig. 2, the atomic Pd–shell layers of the octahedral bimetallic nanoparticles were observed in the thickness of 6 ± 1 monolayers (2.64 nm) and 5 ± 1 monolayers (2.20 nm). In a core–shell structure, the Pd shell included a number of Pd atomic monolayers. The shell layer displayed up to several dozen atomic monolayers, depending on the total volume and concentration of Na_2PdCl_4 . The Pt–Pd core–shell bimetallic nanoparticles showed the number of Pd atomic monolayers in the 20-monolayer regime. Moreover, Fig. 2 also shows a good octahedral Pt–Pd core–shell morphology; however, these particles have truncated polyhedral corners. It is clear that Pt–Pd core–shell nanoparticles also displayed arrangements of highly symmetric atomic columns at their surfaces. The nucleation and growth mechanism of Pt–Pd core–shell nanoparticles were considered in the homogeneous nucleation and growth of both the core and the shell. In addition, the observed morphologies of the Pt–Pd core–shell nanoparticles are strongly dependent on their crystal orientation and the technique limitations of high resolution TEM at approximately 2 nm. In the other hand, the Pt core nanoparticles show the most characteristic morphologies, including tetrahedral, cubic, and octahedral shapes. The formations of their truncated corners were also observed. However, the simultaneous nucleation and growth of various polyhedral nanoparticles need to be further studied. Moreover, the Pd monolayer shells were well grown with similar low-index planes of $\{111\}$, $\{100\}$, and $\{110\}$ or Pd $\{hkl\}$, which are the same as the Pt cores with low-index planes of $\{111\}$, $\{100\}$, and $\{110\}$ or Pt $\{hkl\}$. It was suggested that small Pd nanoclusters were formed and directly deposited onto the surfaces of the Pt cores. The single-crystal Pd nanoshells were grown from these small Pd nanoclusters that matched the surfaces of the single crystal Pt cores, exhibiting sharp polyhedral morphology. The reduction of Na_2PdCl_4 at 160 °C promotes not only homogeneous nucleation but also crystal growth of the thin layer of Pd nanoshells on the surfaces of the Pt nanocores [19]. In the nucleation and growth of the single Pd nanoshell crystal, a very thin Pd layer was formed while the nucleation and growth mechanisms of the Pd nanoshells retain and protect the good morphology of the initial Pt nanocores. A layer-by-layer mechanism was identified. The formation of the Pt atomic monolayer is crucial to the controlled synthesis of the

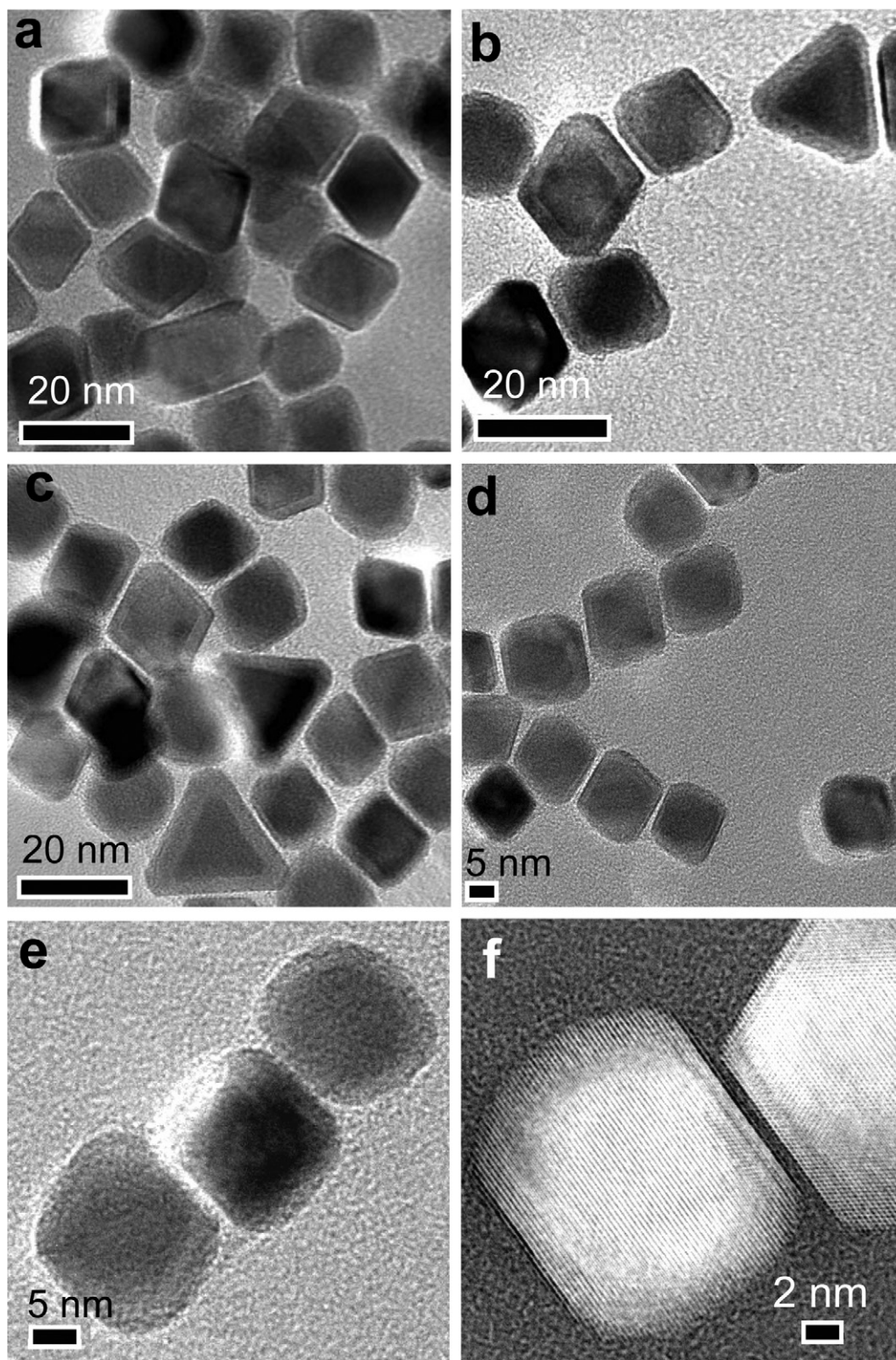


Fig. 2. HRTEM images of Pt–Pd core–shell. The thin Pd shells protect polyhedral Pt cores. The nucleation and growth of Pd shells are controlled by a chemical synthesis. Scale bars: (a)–(c) 20 nm. (d) 5 nm. (e) 5 nm. (f) 2 nm.

bimetallic core–shell nanoparticles. There is a very small lattice mismatch at the transition between the crystalline orientation of the Pt core and that of the Pd shell in the distinctly visible Pt–Pd core–shell geometry observed inside Pt–Pd core–shell nanoparticles (Fig. 2). Thus, high quality Pt–Pd core–shell nanoparticles were achieved.

3.2. Electrocatalytic characterization

3.2.1. Electrochemical reactions

The electrode was swept from $E = -0.2$ to $E = 1.0$ V with respect to the saturated electrode. In Fig. 3, there are seven specific regions in the cyclic voltammogram exhibiting catalytic activity and

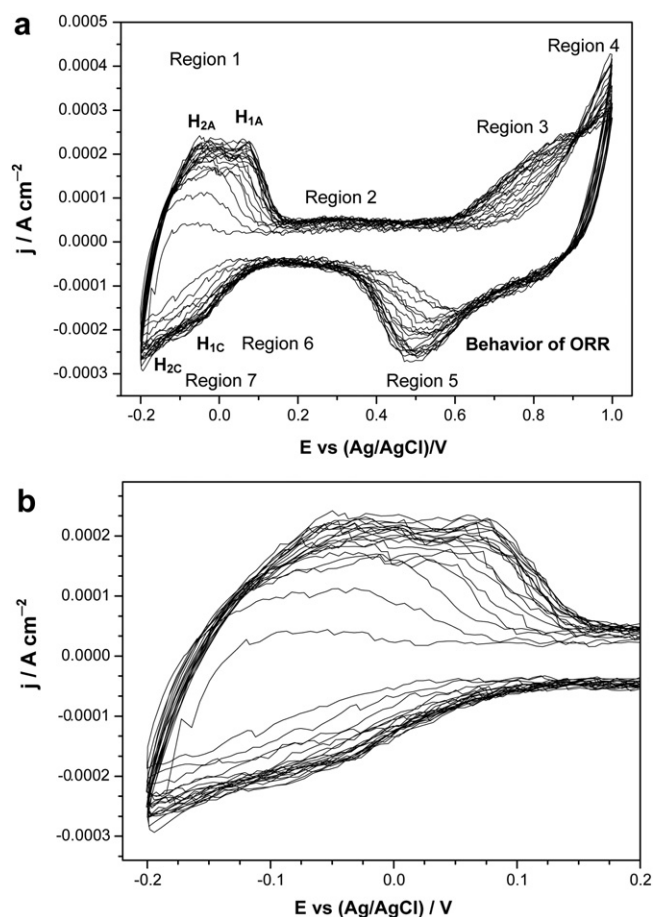


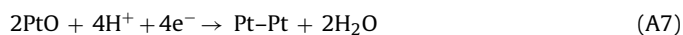
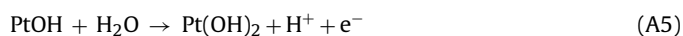
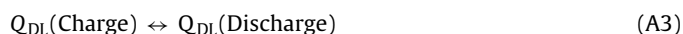
Fig. 3. Cyclic voltammograms of as-prepared Pt nanocatalysts in 0.5 M H₂SO₄ in the ranges of $E = -0.2$ V to $E = 1.0$ V and $E = -0.2$ V to $E = 0.2$ V.

surface kinetics for the case of the Pt nanocatalysts of 4–8 nm. They were characterized by the chemical activity occurring at the electrode surface (Eqs. (A2)–(A8)). In the forward sweep, the first region assigned to hydrogen desorption is crucial. Slow kinetics of hydrogen desorption was confirmed in the cell before the CV stabilization was achieved from the first cycle to the twentieth cycle. We propose to call this process the “slow hydrogen desorption” mechanism to the single metallic nanocatalyst. Here, Q_A is the integrated anodic charge in Coulombs representing the desorption of hydrogen (Eq. (A2)), and Q_C is the integrated cathodic charge representing the adsorption of hydrogen (Eq. (A8)). The atomic hydrogen adsorption charge density can be calculated in Fig. 3. To evaluate the catalytic activity of the prepared nanocatalysts, the electrochemical active surface area (ECSA) of the Pt nanocatalyst is calculated [8,29,30].

$$\text{ECSA} = \frac{Q_H}{0.21 \times L_{\text{Pt}}}, \quad (\text{A1})$$

The regions after the background current subtraction were used to accurately integrate the faradaic contribution. The Q_A/Q_C ratio was characterized by the reversibility of the hydrogen adsorption and desorption reactions on the electrode surface of the prepared Pt nanocatalysts. The specific hydrogen adsorption/desorption regions exhibited various facets at the surfaces of the Pt nanoparticles of low- and high-index planes as well as the effects of their various edges, corners, and terraces [31–34]. In our case, hydrogen adsorption/desorption regions that correspond to the low-index facets are difficult to distinguish in their separate regions. In contrast, the differences were observed in both hydrogen desorption and oxygen adsorption for the low- and high-index

planes. For Pt nanoparticles, the catalytic activity increased in the order of $\{111\} < \{100\} < \{110\}$ or $\{100\} < \{111\} < \{110\}$ planes. These mainly depend on the temperature and type of metal in the nanoparticle-based catalyst [4,31–34]. In addition, the confirmation of H₂ adsorption/desorption by high-index planes was discussed [31–34]. However, researchers need further evidence from both theoretical and experimental studies. The second region showed important characteristics of charging and discharging, which were identified by two double layers of Q_{DL} (charge) and Q_{DL} (discharge) with respect to the standard hydrogen electrode (SHE). The charging and discharging indicated by the double layers during the reverse sweep are the dominant contributors to the current in a half-cell [8,35]. During the in situ CV measurement across a FC, the second region might also contain a limiting hydrogen oxidation current due to hydrogen crossover from the anode chamber during the evaluation of the cathode catalyst [8,35]. Above $E = 0.6$ V, Pt nanocatalysts catalyzed water activation. In our experimental observation, the Pt was covered with an oxide layer at potentials close to $E = 1.0$ V. It was known that the third region showed the formation of Pt–OH and the conversion of Pt–OH into Pt(OH)₂ between $E = 0.8$ V and $E = 1.0$ V. At the same time, the formation of Pt–O and H₂O were seen in the fourth region. Beyond $E = 1.0$ V, the evolution of oxygen gas began to dominate, and a reverse sweep was immediately followed. At potentials close to $E = 0.45$ V, the fifth region showed the formation of Pt–Pt and water. Notably, the slow kinetics of Pt–O reduction was observed in the fifth region. The pathways of Pt oxide reduction were different from the first cycle to the twentieth cycle, and the stabilization of Pt oxide reduction was achieved after the tenth cycle. During the reverse sweep, hydrogen evolution potential was observed in the seventh region, and hydrogen adsorption (Pt–H_{ads}) was observed in the sixth region. The hydrogen evolution potential was $E = -0.2$ V in the seventh region. Hydrogen adsorption–desorption reactions using electrodes in acidic media were discussed in detail [35,36]. The hydrogen evolution reaction (HER) with the Pt catalyst followed the reactions of Volmer, Tafel, and Heyrovsky [6]. The combinations of these reactions were characterized as Volmer–Tafel and Volmer–Heyrovsky mechanisms [6,35,36]. The processes that occurred at the electrode surface exhibiting seven specific regions in cyclic voltammograms follow Eqs. (A2)–(A8).



The seventh region is assigned to hydrogen evolution during the reverse sweep. The hydrogen evolution reaction and hydrogen adsorption on the electrode surface of the Pt–Pd core–shell nanoparticle catalyst showed much better chemical and catalytic activity than the Pt nanocatalyst. The electrode was swept between $E = -0.2$ V and $E = 1.0$ V with respect to the saturated electrode in Fig. 4. Similarly, there were seven specific regions in the cyclic voltammogram, exhibiting catalytic activity and surface kinetics in the case of the Pt–Pd core–shell nanocatalysts (15–25 nm). Notably, Q_A is the integrated anodic charge in Coulombs that represents the desorption of hydrogen, and Q_C is the integrated cathodic charge that represents the adsorption of hydrogen. The charges of Q_A and Q_C showed the chemical activity of catalyst at the surfaces and interfaces of the electrodes and electrolyte. For Pt–M (M = Ru, or

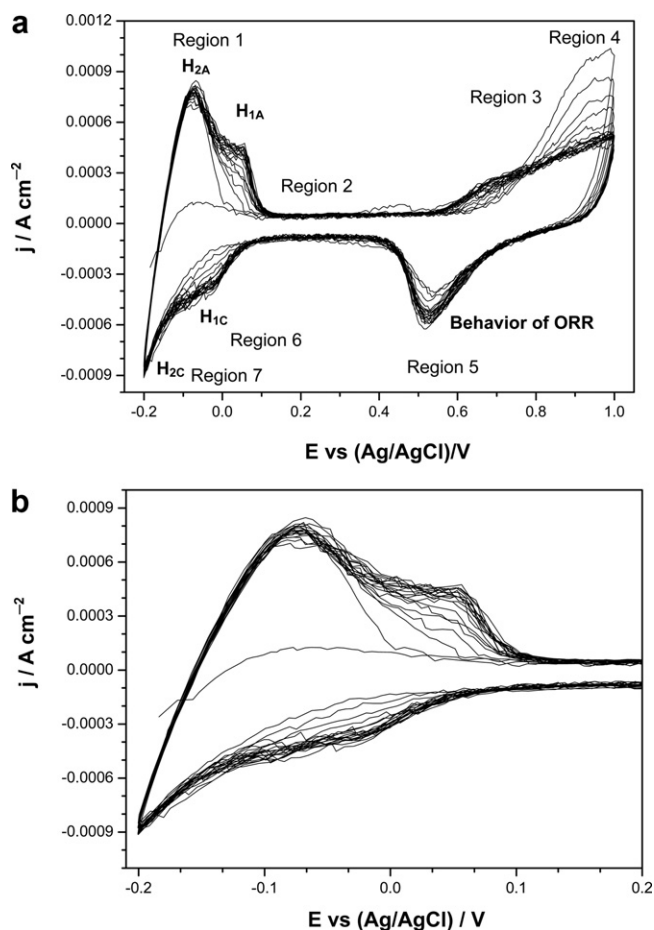


Fig. 4. Cyclic voltammograms of as-prepared Pt–Pd core-shell nanocatalysts in 0.5 M H₂SO₄ in the ranges of $E = -0.2$ V to $E = 1.0$ V and $E = -0.2$ V to $E = 0.2$ V.

Rh, Sn, Pd, . . .), the two specific regions can be distinguished by two anodic (desorption) and two cathodic (adsorption) peaks consisting of H_{1A}, H_{2A}, H_{1C} and H_{2C}, respectively. These peaks are interpreted by the strength of the bonded hydrogen atoms [37,38]. In the hydrogen desorption region, the peak at the more negative potentials (H_{2A}) is attributed to the hydrogen desorption from the bulk of the metal in combination with the desorption of hydrogen adsorbed on the surface. The peak obtained at more positive potentials (H_{1A}) is attributed exclusively to the adsorbed hydrogen [37,38]. In our results, for the case of Pt nanocatalysts, the H_{1A} and H_{2A} peaks were not clearly distinguished after achieving the stabilization of hydrogen desorption in the case of the Pt nanocatalyst. Similarly, the H_{1C} and H_{2C} peaks in the region were also not clearly distinguished. Therefore, Pt–H_{ads} can be both weakly and strongly bonded hydrogen atoms. Therefore, we need to create new active sites on the surfaces of the nanocatalysts because they can give the strongest hydrogen desorption and enhancement of hydrogen desorption. Our proposal of improving Pt-based catalysts is to create new, strongly bonded hydrogen atoms to increase the region of hydrogen desorption. At the same time, ORR activity should be necessarily maintained for the enhancement and stabilization of ORR kinetics.

In Figs. 3–5, the ORR on the electrode of the prepared Pt nanocatalyst is observed as being sluggish [39,40]. In contrast, the fast enhancement of ORR on the electrode of the prepared Pt–Pd core-shell nanocatalyst is clearly observed. Therefore, it is important to use core-shell bimetallic nanocatalysts to increase the ORR rate in the electrode catalyst. For the case of Pt–Pd core-shell nanocatalysts, the H_{1A} and H_{2A} peaks were clearly distinguished

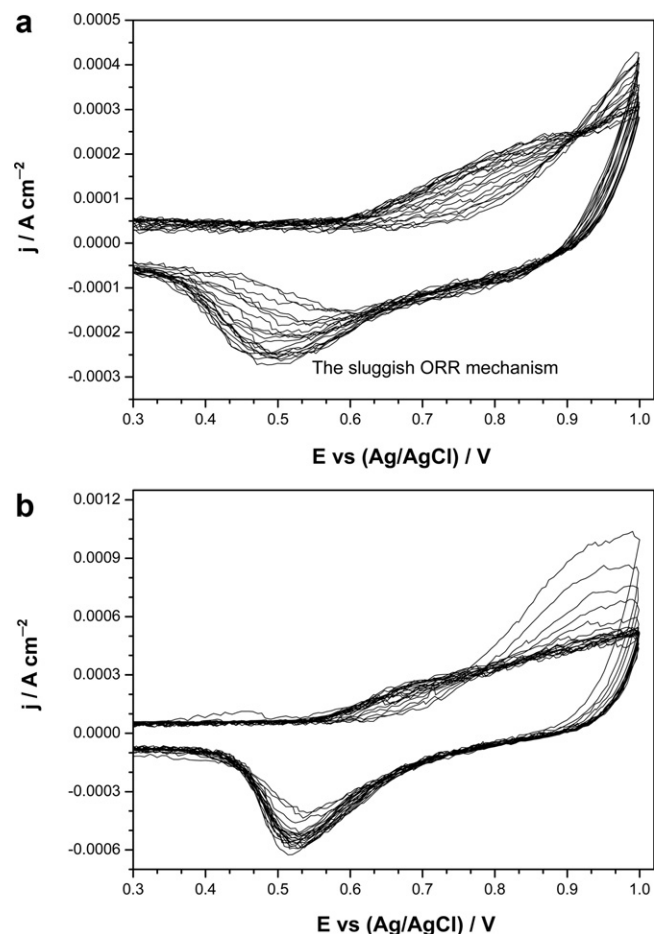


Fig. 5. Cyclic voltammograms of as-prepared Pt and Pt–Pd core-shell nanocatalysts in 0.5 M H₂SO₄ in the range of $E = 0.3$ V to $E = 1.0$ V.

after achieving good stabilization of the fast hydrogen-desorption response and high sensitivity in our results after reaching the stable characterization after only the first cycle. Similarly, the H_{1C} and H_{2C} peaks in the region were also clearly distinguished. Therefore, the electrode with Pd–H_{ads} and/or Pt–Pd–H_{ads} surface monolayers exhibited two types of weakly and strongly bonded hydrogen atoms. The H_{2A} and H_{2C} peaks showed evidence of strongly bonded hydrogen atoms within the sites. This is an important remark for the case of Pt–Pd core-shell nanocatalysts with Pd nanoshells as atomic monolayers in our study. This enables the realization of robust and efficient Pt- or Pd-based core-shell nanocatalysts that are extremely sensitive to the fast hydrogen desorption. The alternative method of improving the hydrogen reaction by core-shell morphology can be realized. Similarly, Q_A was used to accurately integrate the faradaic contribution after the background current subtraction. In addition, the Q_A/Q_C ratio showed the reversibility of the hydrogen adsorption and desorption reactions.

Figs. 4 and 5 showed the first region describing different processes that occurred at the electrode surface. Hydrogen desorption occurred at the anode containing Pt–Pd core-shell nanocatalysts. These processes indicated the formation of a Pt–Pd–H_{ads} layer at the electrode. The hydrogen desorption was very good after only one or two cycles. This shows the excellent hydrogen desorption of the Pt–Pd core-shell configuration, and we call this process “fast hydrogen desorption” or “fast response of hydrogen desorption”. The strong sensitivity and activity of hydrogen desorption is clear evidence, and we hypothesize that the high sensitivity and activity are due to the synergistic effect of the core-shell bimetallic nanoparticles [7]. This possibility represents a progress in electrocatalysis

research. Thus, it can be concluded that Pt–Pd nanocatalysts accelerate the rate of the chemical reaction in hydrogen desorption. It is obvious that the chemical nature of the nanostructure, morphology and size effects of metallic and bimetallic nanoparticles in the nanocatalysis were very different. In the second region, charging and discharging demonstrated good performance and stability. This second region of Pt–Pd nanocatalyst (Fig. 4) from $E = 0.1$ V to $E = 0.4$ V was much more stable than that of the Pt nanocatalyst (Fig. 3) from $E = 0.15$ V to $E = 0.3$ V. Therefore, the prepared Pt–Pd core–shell nanocatalysts showed good stabilization of the relationship between charging and discharging. Above $E = 0.6$ V, Pt–Pd core–shell nanocatalysts also catalyzed water activation. However, the kinetics of their catalysis of water activation was very different from Pt nanocatalysts in Fig. 3. Certainly, the catalysis of water activation of Pt–Pd core–shell nanocatalysts was much better than that of Pt nanocatalysts. It was assumed that Pt–Pd core–shell nanocatalysts are covered with an oxide layer at the maxima close to $E = 1.0$ V. We assumed that these were in the form of Pd–O and/or (Pt–Pd)–O monolayers because the Pd nanoshell monolayers were very thin (less than 20 atomic monolayers). In general, we assigned them to be (Pt–Pd)–O monolayers. Between $E = 0.8$ V and $E = 1.0$ V, the formation and variation of Pt–OH (or Pd), Pt–(OH)₂ (or Pd), and Pt–O (or Pd) with water were determined. In our results, the third region showed the formation of Pd–OH and the conversion of Pd–OH into Pd–(OH)₂ and/or the formation of (Pt–Pd)–OH and the conversion of (Pt–Pd)–OH into (Pt–Pd)–(OH)₂. At the same time, the formation of Pd–O and/or (Pt–Pd)–O and water were seen in the fourth region. In contrast, a new phenomenon was observed in the fourth region, in which the current density was very high during the first cycle. The stability of positive current density was achieved after cyclic voltammetry. At potentials close to $E = 0.52$ V, the fifth region showed the formation of Pd–Pd and/or Pt–Pd–Pd and water. Notably, the fast response and stable kinetics of the Pd and/or Pt–Pd oxide reduction was observed (fifth region). The pathways of Pt or Pt–Pd oxide reduction were different from the first cyclic voltammogram to the twentieth cyclic voltammogram (CV) in the values of current density and voltage; however, their CV curve forms were similar in appearance. The stabilization of Pd and/or Pt–Pd oxide reduction was achieved after only three cyclic voltammograms, which showed better ORR characterization. During the reverse sweep back to the hydrogen evolution potentials in the seventh region, the following surface reactions took place. These showed hydrogen adsorption (Pt–H_{ads} or Pt–Pd–H_{ads}) in the sixth region. The limitation of hydrogen evolution potentials was at a more negative potential close to $E = -0.2$ V; however, the absolute current density was negative. Through the importance of studying electrochemical reactions in detail, the performance of new Pt-based catalysts can be significantly improved.

3.2.2. Comparison of catalytic activity

Fig. 6 shows the cyclic voltammograms of the Pt nanocatalysts (wine color) and Pt–Pd nanocatalysts (line: magenta color) acquired at 50 mV s^{-1} in $0.5 \text{ M H}_2\text{SO}_4$. The voltammograms display the typical shape for base voltammetry. Beyond $E = 0.4$ V in the forward sweep, the Pt–O formation is observed, and its corresponding reduction is given by the negative peak in the backward sweep. In the case of bimetallic nanoparticles, catalytic activity is determined and enhanced by the electronic tuning on the surface of the first metal core brought about by the adsorbed second metal. Such a mechanism may be optimized by controlling the shell thickness and the choice of the second metal as well as the nanoparticle-shape dependence and stability [41,42]. The specific charge transfer (Q_H) due to hydrogen adsorption and desorption is given by: $Q_H = (Q_T - Q_{DL})/2$, where Q_T denotes the total amount of charge during hydrogen adsorption and desorption on Pt sites and Q_{DL} relates to the charge due to the double layer capacitance [7,8].

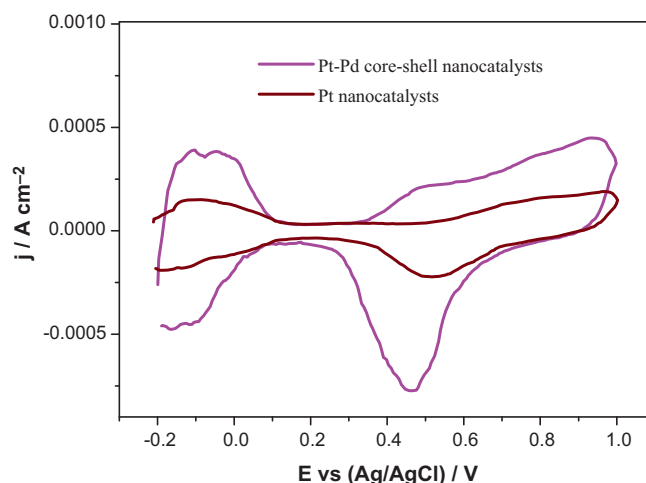


Fig. 6. Cyclic voltammogram of Pt nanocatalysts (a), and Pt–Pd core–shell nanocatalysts (b) on glassy carbon electrode in N_2 -bubbled $0.5 \text{ M H}_2\text{SO}_4$ electrolyte (scan rate: 50 mV s^{-1}).

The area within the curve in the relevant region can give Q_T and Q_{DL} and can be obtained by taking the area under the same region but with the upper and lower boundaries as horizontal lines passing on a data point outset of the hydrogen desorption/adsorption waves. The electrochemical surface area (ECSA) is calculated with Eq. (A1) [8,29,30]. The conversion factor of ~ 0.21 (in mC cm^{-2}) was used for a monolayer of hydrogen. L_{Pt} corresponds to the loading of the catalyst on the glassy carbon surface (in mg cm^{-2}). We have presented the calculated ECSA values of the two samples (Pt nanocatalysts and Pt–Pd core–shell nanocatalysts). The results showed a significant difference in ECSA values between the Pt nanocatalyst and Pt–Pd core–shell nanocatalyst. The Pt–Pd core–shell nanocatalysts exhibited a high value for ECSA ($27.7 \text{ m}^2 \text{ g}^{-1}$), while the Pt–nanocatalysts had a much lower value ($10.5 \text{ m}^2 \text{ g}^{-1}$). These highlighted the main contributing factors for the improvement and fine-tuning of the nanoparticle surface. Therefore, Pt–Pd core–shell nanocatalysts exhibiting efficient electrocatalysis are considered to replace Pt–Ru electrocatalysts with low Pt content for formic acid electro-oxidation [43,44]. Additionally, core–shell electrocatalysts with Pt shell monolayers on Pd₃Co cores significantly enhanced the durability of the ORR activity [44]. In this regard, ternary Pt–Fe–Co alloy electrocatalysts of Pt₈₅Fe₁₀Co₅ formed by electrodeposition showed mass activities that were 3.5 times higher than that of pure Pt nanocatalysts [45]. In particular, the amount of Pt and Pd used (two Pd atomic layers and a Pt atomic half-monolayer) is very small; however, they exhibit very high activity for the electro-oxidation of formic acid [46]. A small amount of Pt deposited on the PdCo–Pd/C core–shell nanoparticles indicated that the core–shell nanoparticles decorated by Pt displayed enhanced stability and electrocatalytic activity for ORR activity [47]. Interestingly, a combination of two types of Pd and Pt nanoparticles (Pd on cubic Pt seeds) for investigation of electrocatalytic formic acid oxidation showed much less self-poisoning and a lower activation energy relative to Pt nanocubes [48]. Indeed, the method uses a combination of mixed metal Pt monolayer electrocatalysts to improve the ORR kinetics relative to the pure Pt nanocatalyst. Its origin was the Pt islands or small clusters or monolayers on the Pd nanoparticles (Pd islands or clusters or monolayers on Pt nanoparticles) [49]. There is still some debate over the potentially stronger enhancement of Pt alloy electrocatalysts for the ORR [50]. At present, we cannot confirm their catalytic characterization and stabilization with certainty and cannot determine whether the prepared nanocatalysts are better than the bimetallic catalysts (e.g., Pt–Pd, Pt–Cu, Pt–Ru) as multi-component alloy nanocatalysts. In addition, the syntheses

of the nanocatalysts show high complexity in confirming their various compositions, sizes, nanostructures, and characterizations. To demonstrate the difference of catalytic activity between two types of metallic and bimetallic systems during a typical catalyst-assisted reaction, cyclic voltammetry in methanol electro-oxidation was performed. To change the ORR property, Pt-based catalysts, such as Pd–Pt and Pd–Pt–Ni electrocatalysts (binary and ternary compositions), or catalysts with non-Pt compositions were tested with the rotating disk electrode (RDE); however, there was no clear experimental proof of higher activity in ORR compared to the binary alloys [51]. In addition, the method of using RDE may possibly lead to a high solubility of nanocatalysts in the electrolytes. To improve the ORR property, Pt–Pd nanocatalysts ($\text{Pt}_x\text{Pd}_{1-x}$ -based nanocatalysts) supported on various carbon nanomaterials (carbon nanotubes (CNTs) such as single-walled CNTs (SWCNTs) or multi-walled CNTs (MWCNTs)) showed high surface area and stability [52]. In addition, Pt–CO poisoning or CO-stripping voltammetry causes a significant decrease in the overall efficiency of DMFCs. Therefore, CO poisoning should be controlled at a low CO tolerance [2,10]. Pt–M (M=Co, Ni, Mn, or Fe, etc.) or ternary Pt-base alloys were prepared in an effort to find highly active surfaces and sites. Their usefulness in PEMs was reduced because of the dissolution of Co, and Ni into the solution during the operation of the FCs. This led to the conclusion that multi-composition nanocatalysts are less desirable because of the high complexity in the preparation and application [53]. Moreover, quaternary Pt–Ru–Os–Ir alloy nanocatalysts or multi-metallic nanocatalysts showed slightly better electrocatalytic activity than Pt–Ru nanocatalysts; however, its preparation procedure was much more complex [54,55]. Based on the density functional theory in surface chemistry and catalysis, Pt–Pd catalysts are great candidates in catalysis [56]. The main reasons are the high oxygen reduction activity of Pt and Pd metal catalysts because they are confirmed in their activity to be on the top of the volcano curve among transition metals, such as Ir, Cu, and Ag, for obtaining high ORR activity [56,57]. Among the noble metals, the four metals Pd, Pt, Rh, and Ir were confirmed to have high adsorption energy characterization. Accordingly, the Pt_3M catalysts (M= Ni, Co, Fe, Ti) showed their catalytic activity vs. the d-band center. According to DFT theory, the volcano-shaped dependency was presented in the best electrocatalytic activity of Pt_3Ni , comparable to that of Pt_3Co in this experiment [39]. At present, the appropriate approach for improving the catalytic surface and reducing the loading of the Pt-catalyst is to produce novel Pd or Pt based core-shell bimetallic nanocatalysts using Pt monolayers (nanoshells) or Pd monolayers (nanoshells), with a strong interest in Pt–Ru, Pt–Cu bimetallic nanoparticles. The core-shell nanostructures of Pt-based electrocatalysts have been introduced in various solutions [58]. This is meaningful in the continuous efforts of the design of Pt or Pd nanoshells with one or more atomic multi-monolayers [59]. The innovative solutions of Pt monolayers on the definite cores in the nanosized ranges have been highly evaluated because the cores can be rich and diverse in materials such as metal, bimetal, alloy, and glass, as well as multi-composition materials [60,61]. In addition, the cost of Pd is around 20% of the cost of Pt per weight, leading to a significant reduction of the Pt loading. Importantly, the ORR of Pd metal is very close to that of Pt metal in their catalytic activity [62]. At present, a great deal of research in the preparation of the electrocatalysis of Pt–Pd alloy nanocatalysts or Pt–Pd alloy nanocatalysts with or without various supports has been reported [63,64]. Recently, Pt-based alloy nanocatalysts (Pt–M, M=Co, Fe, Ni, Pd) with cubic and octahedral morphologies have been prepared. For example, cubic and octahedral Pt_3Ni catalysts exhibited higher ORR activity than that of Pt/C, showing one of the highest known values of ORR activity [65]. A new hydrogen adsorption site in the hetero-interface between the Pd core and Pt shell of the Pd–Pt core-shell nanoparticle has been studied to improve hydrogen storage [66].

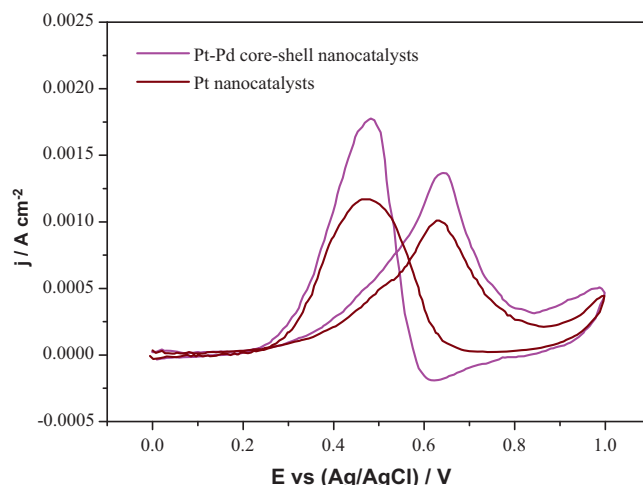


Fig. 7. Cyclic voltammograms towards methanol electro-oxidation of Pt nanocatalyst and Pt–Pd nanocatalyst.

In electrochemical measurements, the electrolyte solution is 0.5 M H_2SO_4 + 1.0 M CH_3OH , and a scan rate of 50 mV s^{-1} was used. Fig. 7 shows a comparison of the cyclic voltammograms between the Pt nanocatalysts and Pt–Pd core-shell nanocatalysts in the mixture of 0.5 M H_2SO_4 and 1 M CH_3OH . A stable voltammogram was attained after 20 cycles of sweeping between 0 and 1 V. Two oxidation peaks are noticeable; the first one is between $E=0.6 \text{ V}$ and $E=0.8 \text{ V}$ in the forward sweep, and the other is between 0.4 and 0.5 V in the backward sweep. The two peaks are directly related to methanol oxidation and the associated intermediates. Moreover, the curve shape is in excellent agreement with other publications [67–69]. The shoulder at $E \sim 0.8 \text{ V}$ relates to the complete oxidation of intermediates, causing the current to rise again at a higher potential. To explain clearly, the anodic current decreased significantly when the voltage was raised beyond the peak current potential because of the blocking effect by the adsorbed intermediate species on the active sites. Afterward, the anodic current increased again because the concentration of available active sites increased and the methanol molecules were oxidized again. In the backward scan, the second peak is related to the removal of the carbonaceous products from the forward scan. The peak current density in the forward scan (i_f) is commonly associated with the catalytic activity for methanol electro-oxidation. For the fabricated catalyst samples, there is a significant difference in the magnitude of i_f as well as their corresponding voltage values. The high value of i_f is observed for Pt–Pd core-shell nanocatalyst ($j = 1.5 \times 10^{-3} \text{ A cm}^{-2}$). This current response is located more negatively ($E_f = 0.63 \text{ V}$) in terms of $E \text{ vs. (Ag/AgCl)/V}$ than the rest, indicating the most effective catalyst for the oxidation of methanol molecules. Based on other reports, the obtained results are comparable considering that no carbon support was used and some inaccessible catalyst sites could be present during measurement [70]. In some recent works, Pt–Pd alloy electrocatalysts or Pt–Pd alloy electrocatalysts supported on various carbon nanomaterials have been developed for methanol tolerant oxygen reduction as well as for an improvement of catalytic activity and stability in methanol electro-oxidation, especially for the stability of the core-shell structure [71,72]. Moreover, Pd–Pt alloyed structures such as solid-solution alloys possess enhanced hydrogen-storage capacity. The structures of Pd–Pt alloys were reconstructed from the core-shell configuration through hydrogen adsorption and desorption [73]. Therefore, we can use Pt–Pd core-shell nanocatalysts with shells fabricated with Pt monolayers or Pd monolayers. Pt–Pd core-shell nanocatalysts are less expensive and can replace the present technology of Pt–Ru nanocatalysts

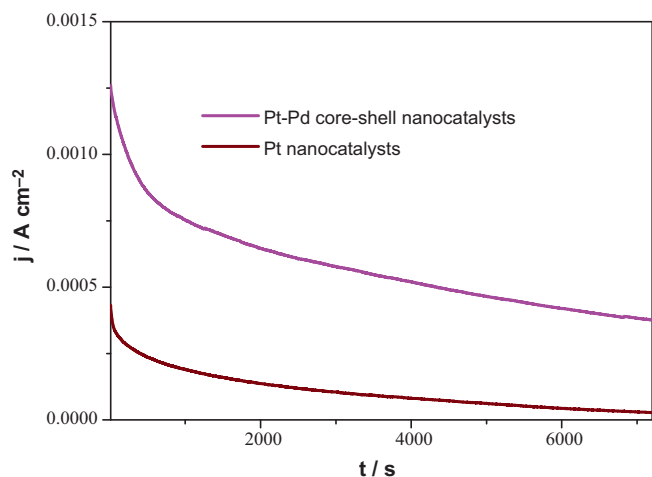


Fig. 8. Chronoamperometry data of Pt and Pt–Pd nanoparticles. Electrolyte solution of 0.5 M H_2SO_4 + 1.0 M CH_3OH and polarization potential about $E = 0.5$ V.

in the development of DMFC applications [74,75]. At the same time, the electrocatalytic activity and selectivity of the Pt–Pd core–shell nanocatalysts must be intensively studied to realize the DMFCs with respect to the membrane electrode assembly (MEA) technology [9,10]. At present, DMFCs can work appropriately between the temperatures of 30 and 110 °C with various proton exchange membranes, such as Nafion 117, as the electrolyte for methanol oxidation at the electrode surface. Fig. 8 shows the chronoamperometry results taken from the Pt and Pt–Pd nanocatalysts. The polarization potential was $E = 0.5$ V and was held over a period of 2 h. Based on this graph, the Pt–Pd core–shell nanocatalysts ($t = 15$ min) exhibited an excellent current response much higher than that of Pt nanocatalysts throughout the measurement. As the polarization progressed, intermediate species accumulated on the accessible catalytic sites. In effect, it was expected that the current response would decline over time because of two likely reasons. The first suggests that the stripping of intermediates is usually slower than the rate at which methanol molecules are oxidized, and the second showed that nanoparticles usually undergo particle coarsening during work operation [76]. However, these can be improved if a second metal is incorporated and an optimum configuration is achieved. In the case of the two samples, a stable characterization was observed for Pt–Pd core–shell nanocatalysts. They showed a very high initial current of $j = 1.29 \times 10^{-3} \text{ A cm}^{-2}$ with 30.01% current left after 2 h of polarization. Meanwhile, the Pt catalyst exhibited the highest retained current of 3.67%, although its initial current of $j = 4.33 \times 10^{-4} \text{ A cm}^{-2}$ is much lower. Recently, Pt–Pd nanoparticles and their nanoalloying catalysts on various commercial carbon black and multi-walled carbon nanotubes (MWCNs) have been prepared in DMFCs. Importantly, these nanocatalysts could be easily recovered from their final reaction solution via a conventional filtration [77]. In addition, Pt–Pd nanocatalysts will become a suitable choice of replacing Pt–Ru nanocatalysts and reducing the high cost of Pt loading [78]. Because of their importance, Pt–Pd bimetallic nanoparticles prepared by the polyol method were intensively investigated to show their high activity for ORR [79–81]. Our next studies will emphasize the problems of Pt-based multi-composition nanocomposite catalysts.

Fig. 9 shows the two XRD patterns of the prepared Pt and Pt–Pd core–shell nanoparticles. The results showed a crystalline Pt face centered cubic (fcc) phase. The peaks were characterized by (1 1 1), (2 0 0), (2 2 0), (3 1 1), and (2 2 2) peaks corresponding to 2θ values of ~ 40.9 , 46.4, 67.9, 81.8, and 86.2°, respectively [20]. Therefore, the results are the agreement with the TEM data. Two XRD patterns of Pt and Pt–Pd core–shell nanoparticles showed the same

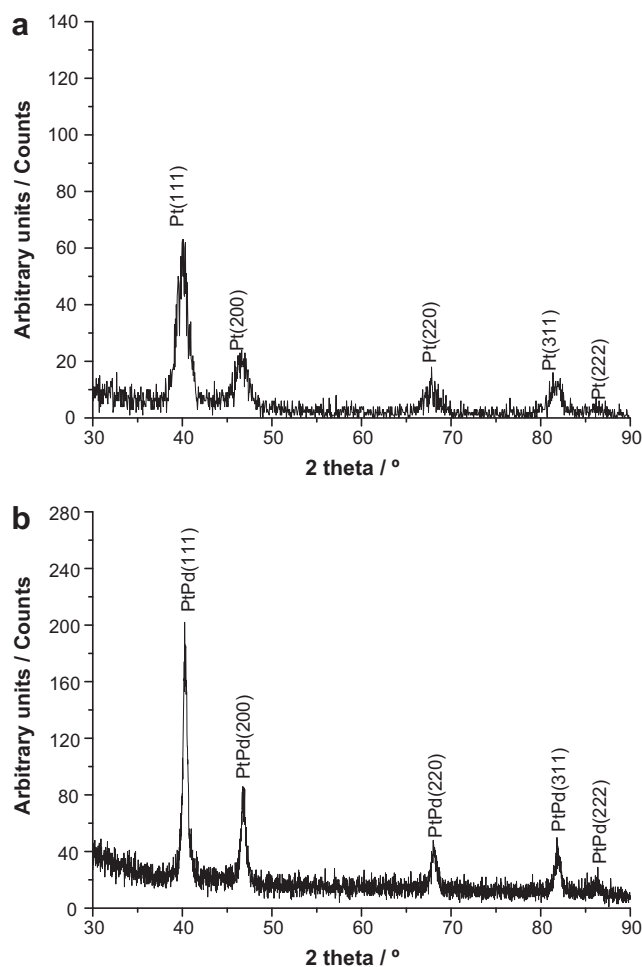


Fig. 9. XRD patterns of (a) polyhedral Pt nanoparticles, and (b) Pt–Pd core–shell nanoparticles.

appearance and shape; however, their intensities and peak positions were different. The (2 0 0) peaks indicated the alignment of Pt and Pt–Pd core–shell nanoparticles of a narrow shape distribution on the planar substrate. The XRD peaks of the Pt nanoparticles were broad and comparable to those of the corresponding bulk Pt material in a system of (1 1 1), (2 0 0), (3 1 1), (2 2 2), (4 0 0), (3 3 1), (4 2 0), (4 2 2), (3 3 3), (5 1 1) or more (hkl). By using one XRD peak, the average size of the Pt nanocrystallites can be calculated by the width of the reflection according to the Debye–Scherrer equation: $D = 0.9\lambda/(\beta \cos \theta)$, where β is the full width at half maximum (FWHM) of the peak, θ is the angle of diffraction, and λ is the wavelength of the X-ray radiation. Here, the (2 2 0) reflections of Pt nanoparticles were used to calculate the crystallite size.

4. Conclusions

In this study, we controllably synthesized polyhedral Pt nanoparticles and Pt–Pd core–shell nanoparticles via a modified polyol method using AgNO_3 . The overgrowth of the thin Pd nanoshells on the Pt nanocores due to epitaxial growth mode was observed. We predicted that Pt–Pd core–shell nanoparticles were formed in both the FM and SK growth modes. In particular, the core–shell nanoparticles with a thin Pd monolayer shell demonstrated potential as an electrocatalyst with great stabilization and reliability, far exceeding Pt nanoparticles with the same polyhedral morphologies.

Acknowledgements

We thank the Institute of Ceramics Research and Education (ICRE) and the Nagoya Institute of Technology (NITECH) for supporting our research program in science and nanotechnology in Japan. We also thank the Kyushu University, the Novel Carbon Resources Sciences, the Kyushu University Global GOE Program for kind support and help.

References

- [1] A. Chen, P. Holt-Hindle, *Chem. Rev.* 110 (2010) 3767.
- [2] E. Antolini, *Energy Environ. Sci.* 2 (2009) 915.
- [3] A.A. Gewirth, M.S. Thorum, *Inorg. Chem.* 49 (2010) 3557.
- [4] Z. Peng, H. Yang, *Nano Today* 4 (2009) 143.
- [5] R.R. Adzic, J. Zhang, K. Sasaki, M.B. Vukmirovic, M. Shao, J.X. Wang, A.U. Nilekar, M. Mavrikakis, J.A. Valerio, F. Uribe, *Top. Catal.* 46 (2007) 249.
- [6] N.M. Markovic, P.N. Ross, *Surf. Sci. Rep.* 45 (2002) 117.
- [7] B. Corain, G. Schmid, N. Toshima, *Metal Nanoclusters in Catalysis and Materials Science: The Issue of Size Control*, Elsevier, Amsterdam, 2004.
- [8] S. Basu, *Recent Trends in Fuel Cell Science and Technology*, Anamaya Publishers, New Delhi, India, 2007.
- [9] S. Bose, T. Kuila, T.X.H. Nguyen, N.H. Kim, K. Lau, J.H. Lee, *Prog. Polym. Sci.* 36 (2011) 813.
- [10] E. Antolini, *Appl. Catal. B* 88 (2009) 1.
- [11] A.M. Zainoodin, S.K. Kamarudin, W.R.W. Daud, *Int. J. Hydrogen Energy* 35 (2010) 4606.
- [12] S. Alayoglu, A.U. Nilekar, M. Mavrikakis, B. Eichhorn, *Nat. Mater.* 7 (2008) 333.
- [13] B.G. Pollet, *Int. J. Hydrogen Energy* 35 (2010) 11986.
- [14] H. Yang, *Angew. Chem. Int. Ed.* 50 (2011) 2.
- [15] K. Sasaki, J.X. Wang, H. Naohara, N. Marinkovic, K. More, H. Inada, R.R. Adzic, *Electrochim. Acta* 55 (2010) 2645.
- [16] Y. Wang, N. Toshima, *J. Phys. Chem. B* 101 (1997) 5301.
- [17] D. Kaplan, M. Alon, L. Burstein, Y. Rosenberg, E. Peled, *J. Power Sources* 196 (2011) 1078.
- [18] H. Wang, C. Xu, F. Cheng, M. Zhang, S. Wang, S.P. Jiang, *Electrochem. Commun.* 10 (2008) 1575.
- [19] N.V. Long, N.D. Chien, T. Hayakawa, H. Hirata, G. Lakshminarayana, M. Nogami, *Nanotechnology* 21 (2010) 035605.
- [20] H. Song, F. Kim, S. Connor, G.A. Somorjai, P. Yang, *J. Phys. Chem. B* 109 (2005) 188.
- [21] N. Tian, Z.Y. Zhou, S.G. Sun, *J. Phys. Chem. C* 112 (2008) 19801.
- [22] M. Subramannia, V.K. Pillai, *J. Mater. Chem.* 18 (2008) 5858.
- [23] K. Lee, M. Kim, H. Kim, *J. Mater. Chem.* 20 (2010) 3791.
- [24] C. Susut, T.D. Nguyen, G.B. Chapman, Y. Tong, *Electrochim. Acta* 53 (2008) 6135.
- [25] R. Ferrando, J. Jellinek, R.L. Johnston, *Chem. Rev.* 108 (2008) 845.
- [26] J. Zhang, Y. Tang, K. Lee, M. Ouyang, *Science* 327 (2010) 1634.
- [27] J. Zhang, F.H.B. Lima, M.H. Shao, K. Sasaki, J.X. Wang, J. Hanson, R.R. Adzic, *J. Phys. Chem. B* 109 (2005) 22701.
- [28] L. Carbone, P.D. Cozzoli, *Nano Today* 5 (2010) 449.
- [29] K.R. Cooper, V. Ramani, J.M. Fenton, H.R. Kunz, *Experimental Methods and Data Analyses for Polymer Electrolyte Fuel Cells*, Scribner Associates Inc., 2005.
- [30] Z. Liu, J.Y. Lee, W. Chen, M. Han, L.M. Gan, *Langmuir* 20 (2004) 181.
- [31] R. Gomez, A. Fernandez-Vega, J.M. Felio, A. Aldaz, *J. Phys. Chem.* 97 (1993) 4769.
- [32] N. Furuya, S. Koide, *Surf. Sci.* 220 (1989) 18.
- [33] T.J. Schmidt, V. Stamenkovic, M. Arenz, N.M. Markovic, J.P.N. Ross, *Electrochim. Acta* 47 (2002) 3765.
- [34] Z.L. Wang, *J. Phys. Chem. B* 104 (2000) 1153.
- [35] I. Ávila-García, M. Plata-Torres, M.A. Domínguez-Crespo, C. Ramírez-Rodríguez, E.M. Arce-Estrada, *J. Alloys Compd.* 434 (2007) 764.
- [36] L. Luo, M. Futamata, *Electrochem. Commun.* 8 (2006) 231.
- [37] Y. Lee, A. Ko, S. Han, H. Kim, K. Park, *Phys. Chem. Chem. Phys.* 13 (2011) 5569.
- [38] J. Solla-Gullón, V. Montiel, A. Aldaz, J. Clavilier, *Electrochem. Commun.* 4 (2002) 716.
- [39] Y. Bing, H. Liu, L. Zhang, D. Ghosh, J. Zhang, *Chem. Soc. Rev.* 39 (2010) 2184.
- [40] Y. Qiao, C.M. Li, *J. Mater. Chem.* 21 (2011) 4027.
- [41] Y. Lu, W. Chen, *Chem. Commun.* 47 (2011) 2541.
- [42] A. Lebon, A. García-Fuente, A. Vega, F. Aguilera-Granja, *Phys. Rev. B* 83 (2011) 125427.
- [43] E.A. Baranova, N. Miles, P.H.J. Mercier, Y.L. Page, B. Patarachao, *Electrochim. Acta* 55 (2010) 8182.
- [44] J.X. Wang, H. Inada, L. Wu, Y. Zhu, Y. Choi, P. Liu, W. Zhou, R.R. Adzic, *J. Am. Chem. Soc.* 131 (2009) 17298.
- [45] S.J. Hwang, S.J. Yoo, S. Jang, T. Lim, S.A. Hong, S. Kim, *J. Phys. Chem. C* 115 (2011) 2483.
- [46] P. Fang, S. Duan, X. Lin, J.R. Anema, J. Li, O. Buriez, Y. Ding, F. Fan, D. Wu, B. Ren, Z.L. Wang, C. Amatore, Z. Tian, *Chem. Sci.* 2 (2011) 531.
- [47] D. Wang, H.L. Xin, Y. Yu, H. Wang, E. Rus, D.A. Muller, H.D. Abruña, *J. Am. Chem. Soc.* 132 (2010) 17664.
- [48] H. Lee, S.E. Habas, G.A. Somorjai, P. Yang, *J. Am. Chem. Soc.* 130 (2008) 5406.
- [49] J. Zhang, M.B. Vukmirovic, K. Sasaki, A.U. Nilekar, M. Mavrikakis, R.R. Adzic, *J. Am. Chem. Soc.* 127 (2005) 12480.
- [50] J.R. Croy, S. Mostafa, L. Hickman, H. Heinrich, B.R. Cuenya, *Appl. Catal. A* 350 (2008) 207.
- [51] J. Zhao, A. Manthiram, *Appl. Catal. B* 101 (2011) 660.
- [52] B. Wu, Y. Kuang, X. Zhang, J. Chen, *Nano Today* 6 (2011) 75.
- [53] Y. Sung, J. Hwang, J.S. Chung, *Int. J. Hydrogen Energy* 36 (2011) 4007.
- [54] B. Gurau, R. Viswanathan, R. Liu, T.J. Lafrenz, K.L. Ley, E.S. Smotkin, E. Reddington, A. Sapienza, B.C. Chan, T.E. Mallouk, S. Sarangapani, *J. Phys. Chem. B* 102 (1998) 9997.
- [55] C. Zhong, J. Luo, B. Fang, B.N. Wanjala, P.N. Njoki, R. Loukrakpam, J. Yin, *Nanotechnology* 21 (2010) 062001.
- [56] J.K. Nørskov, J. Rossmeisl, A. Logadottir, L. Lindqvist, J. Kitchin, T. Bligaard, H. Jónsson, *J. Phys. Chem. B* 108 (2004) 17887.
- [57] J.K. Nørskova, F. Abild-Pedersen, F. Studt, T. Bligaard, *Density Functional Theory in Surface Chemistry and Catalysis*, www.pnas.org/cgi/doi/10.1073/pnas.1006652108, pp. 1–7.
- [58] C. Kulp, X. Chen, A. Puschhof, S. Schwamborn, C. Somsen, W. Schuhmann, M. Bron, *Chem. Phys. Chem.* 11 (2010) 2854.
- [59] K. Sasaki, H. Naohara, Y. Cai, Y.M. Choi, P. Liu, M.B. Vukmirovic, J.X. Wang, R.R. Adzic, *Angew. Chem. Int. Ed.* 49 (2010) 8602.
- [60] Y. Xing, Y. Cai, M.B. Vukmirovic, W. Zhou, H. Karan, J.X. Wang, R.R. Adzic, *J. Phys. Chem. Lett.* 1 (2010) 3238.
- [61] A. Yin, Y. Zhang, C. Yan, *J. Am. Chem. Soc.* 133 (2011) 3816.
- [62] B. Lim, M. Jiang, T. Yu, P.H.C. Camargo, Y. Xia, *Nano Res.* 3 (2010) 69.
- [63] X. Zhou, L. Fan, *Electrochim. Acta* 55 (2010) 8111.
- [64] W. He, M. Chen, Z. Zou, Z. Li, X. Zhang, S. Jin, D.J. You, C. Pak, H. Yang, *Appl. Catal. B* 97 (2010) 347.
- [65] J. Wu, A. Gross, H. Yang, *Nano Lett.* 11 (2011) 798.
- [66] M. Yamauchi, H. Kobayashi, H. Kitagawa, *Chem. Phys. Chem.* 10 (2009) 2566.
- [67] S. Jingyu, H. Jianshu, C. Yanxia, Z. Xiaogang, *Int. J. Electrochem. Sci.* 2 (2007) 64.
- [68] S. Wei, D. Wu, X. Shang, R. Fu, *Energy Fuels* 23 (2009) 908.
- [69] K. Kakaei, M. Zhiani, H. Gharibi, *J. Phys. Chem. C* 114 (2010) 5233.
- [70] R.G. Freitas, E.P. Antunes, E.C. Pereira, *Electrochim. Acta* 54 (2009) 1999.
- [71] W. Wang, Q. Huang, J. Liu, Z. Zou, Z. Li, H. Yang, *Electrochem. Commun.* 10 (2008) 1396.
- [72] P. Ercius, T. Duden, V.R. Radmilovic, *Microsc. Microanal.* 16 (2010) 1650.
- [73] H. Kobayashi, M. Yamauchi, H. Kitagawa, Y. Kubota, K. Kato, M. Takata, *J. Am. Chem. Soc.* 132 (2010) 5576.
- [74] M. Carmo, A.R. Santos, J.G.R. Poco, M. Linardi, *J. Power Sources* 173 (2007) 860.
- [75] I. Avila-García, C. Ramirez, J.M.H. Lopez, E.M.A. Estrada, *J. Alloys Compd.* 495 (2010) 462.
- [76] A.M. Remona, K.L.N. Phani, *J. Fuel Cell Sci. Technol.* 8 (2011) 011001.
- [77] X. Chen, H. Wang, J. He, Y. Cao, Z. Cui, M. Liang, *J. Nanotechnol.* 10 (2010) 3138.
- [78] O.A. Petrii, *J. Solid State Electrochem.* 12 (2008) 609.
- [79] B. Lim, J. Wang, P.H.C. Camargo, M. Jiang, M.J. Kim, Y. Xia, *Nano Lett.* 8 (2008) 2535.
- [80] N.V. Long, T. Asaka, T. Matsubara, M. Nogami, *Acta Mater.* 59 (2011) 2901.
- [81] N.V. Long, T.D. Hien, T. Asaka, M. Ohtaki, M. Nogami, *Int. J. Hydrogen Energy* 36 (2011) 8478.